

In Search of the Perfect Free-Kick: An Experimental Investigation of the Magnus Effect and Trajectory Spirals

Théo Palagi

2023

Abstract

This study investigates the aerodynamic mechanisms governing the curved trajectories of spinning spherical projectiles, famously exemplified by the "perfect free-kick" in soccer. The primary phenomenon driving this curvature is the Magnus effect. We approach this problem by first establishing a theoretical framework based on fluid mechanics, transitioning from ideal potential flow models to real viscous flows characterized by drag and turbulence. To validate these models, controlled laboratory experiments were conducted by launching spinning marbles into fluids of varying viscosities (water and oil). A crucial aspect of our data analysis involves the reconstruction of the trajectory from high-speed chronophotography, requiring a discrete summation assumption for the curvilinear abscissa. Our results confirm the exponential decay of translational velocity and allow for the determination of drag coefficients (C_x) in different Reynolds number regimes. Finally, drawing upon the work of C. Clanet, we conclude that the "perfect" trajectory is not merely a circular arc but a sensitive, tightening spiral resulting from the differential decay rates of translational and rotational velocities, making its exact reproduction practically impossible.

1 Introduction

In 1997, during the Tournoi de France, Roberto Carlos struck a free-kick that defied visual expectations. The ball started well outside the goalpost before swerving violently upwards to score. This iconic moment serves as the motivating example for our physical inquiry into curved flight paths.

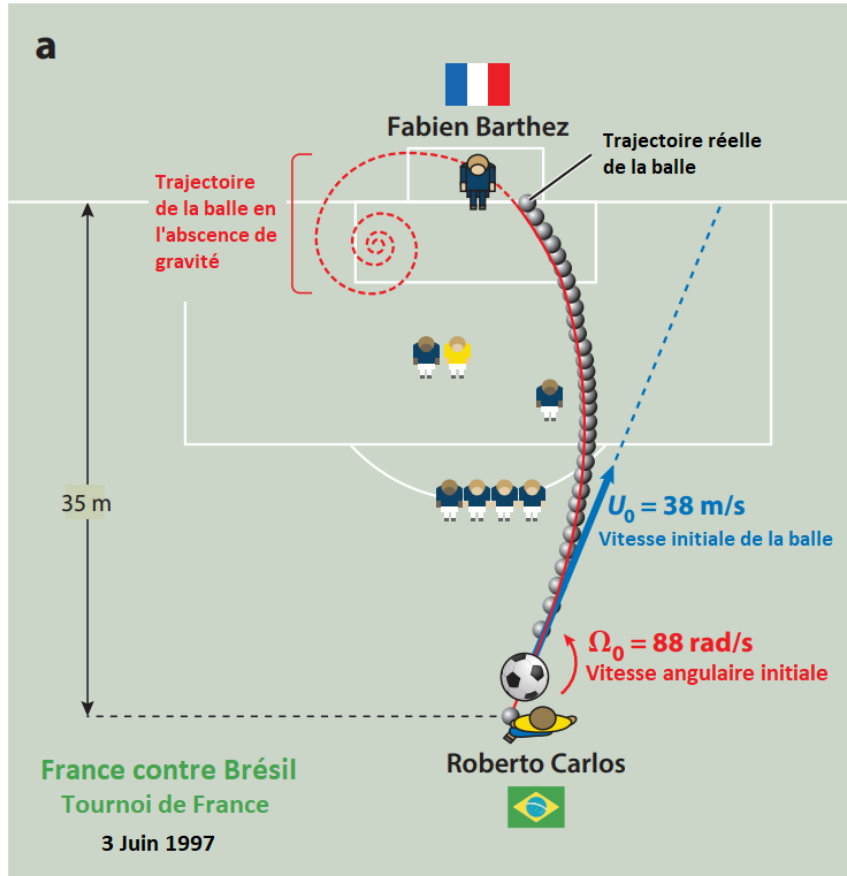


Figure 1: The trajectory of Roberto Carlos' free-kick (1997). Source: C. Clanet, The spinning ball spiral, New Journal of Physics 12.

The problematic central to this research is: **How can one achieve the perfect free-kick?** To answer this, we must move beyond anecdote and analyze the underlying physics. The phenomenon at play is the Magnus effect, where a spinning object moving through a fluid experiences a lateral force.

The complexity of football trajectories has been mapped in "phase diagrams" of aerodynamics, as shown by Clanet et al., highlighting that different combinations of speed, spin, and surface roughness lead to vastly different flight regimes (Fig. 2).

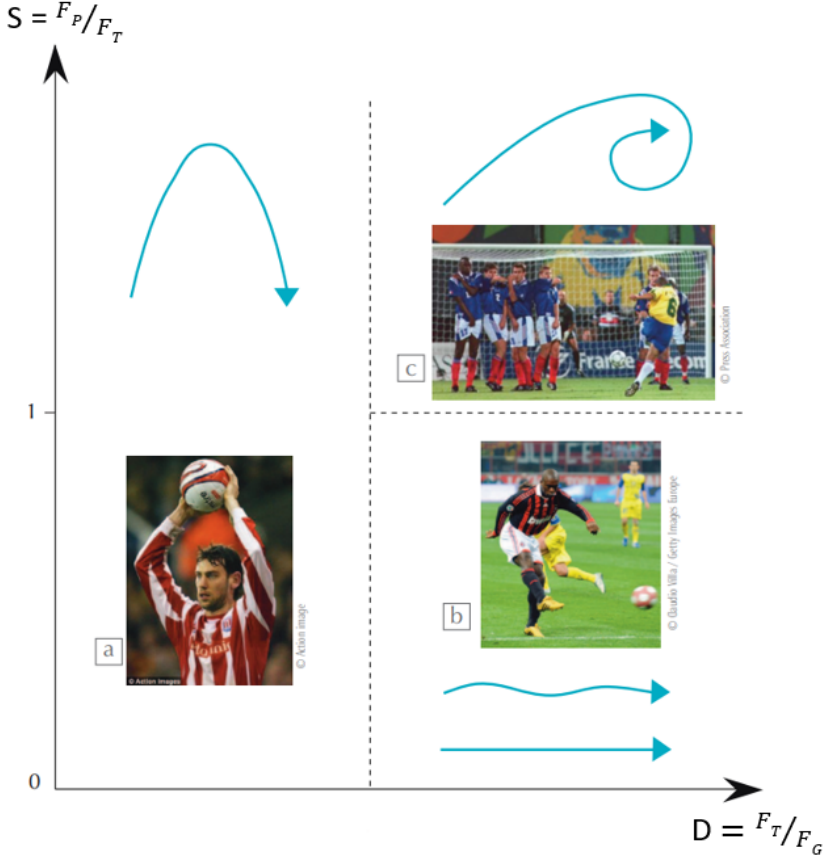


Figure 2: Phase diagram of different trajectories observed in football. Source: Le football et ses trajectoires, C. Clanet.

This paper is structured as follows: Section 2 establishes the theoretical foundation of the Magnus effect, moving from ideal to real fluids. Section 3 details our experimental setup and methodology, specifically justifying our data processing assumptions. Section 4 presents the results of our experiments in water and oil. Finally, Section 5 concludes by explaining the spiral nature of the trajectory and the inherent difficulty of the "perfect" shot.

2 Theoretical Framework

2.1 Approaching the Magnus Effect: Potential Flow

To understand the origin of the lateral force, it is useful to first consider an ideal, irrotational, incompressible, and homogeneous flow around a cylinder (2D approximation of a sphere).

In such a potential flow, the velocity field \vec{V} derives from a potential Φ ($\vec{V} = \vec{\text{grad}}\Phi$). By superimposing a uniform flow V_0 and a vortex of circulation Γ (representing the rotation), we obtain an asymmetric velocity field.

Applying Bernoulli's theorem on a streamline around the object:

$$\frac{P}{\rho} + \frac{V^2}{2} = \text{constant} \quad (1)$$

Where the velocity V is higher (due to rotation adding to the free stream velocity), the pressure P must be lower, and vice-versa. Integrating these pressure differences over the surface leads to the Kutta-Joukowsky lift theorem, giving the Magnus force \vec{F}_p :

$$\vec{F}_p = \rho \vec{V} \wedge \vec{\Gamma} \quad (2)$$

For a cylinder of radius R spinning at angular velocity ω , $\Gamma = -2\pi R^2 \omega$.

We visualized this ideal flow analogy using a Hele-Shaw cell (Fig. 3). In this setup, the mean velocity profile between two close plates creates a potential flow pattern, visually matching theoretical streamlines (Fig. 4).

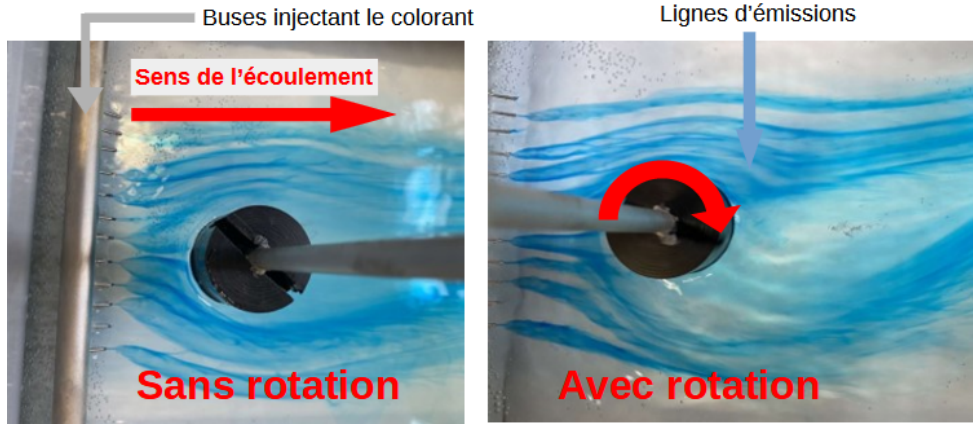


Figure 3: Hele-Shaw cell setup.

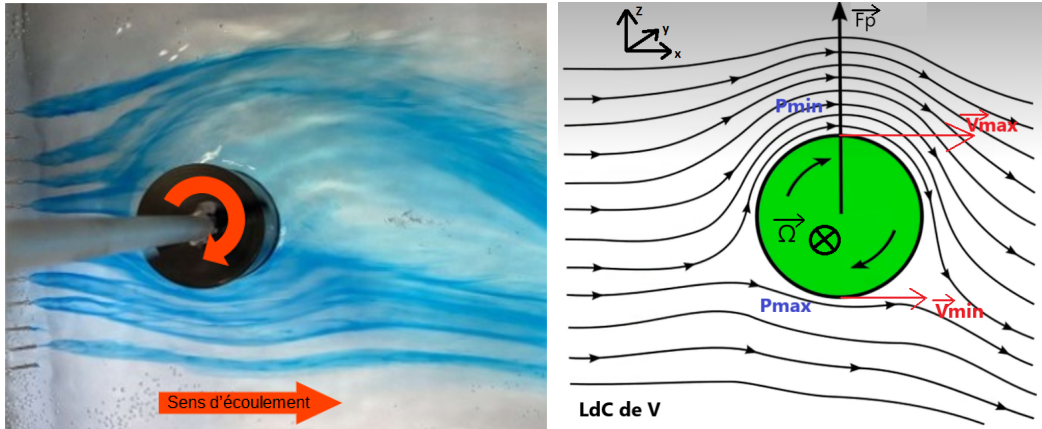


Figure 4: Comparison: Experimental potential flow visualization in Hele-Shaw cell (left) vs. Theory (right).

2.2 Real Fluids and Equation of Motion

In reality, fluids have viscosity η . The flow regime is characterized by the Reynolds number $Re = \frac{\rho U_0 R}{\eta}$. For high Re , the flow is turbulent, and the object experiences a quadratic drag force \vec{F}_T :

$$\vec{F}_T = -\frac{1}{2}\pi\rho C_x R^2 U \vec{U} \quad (3)$$

where C_x is the drag coefficient.

To determine the trajectory's equation, we apply Newton's second law to a sphere of mass m in the lab frame. Projecting onto the tangential direction (velocity vector \vec{U}):

$$m \frac{dU}{dt} = -\frac{1}{2} C_x \pi \rho R^2 U^2 \quad (4)$$

We introduce the curvilinear abscissa s , such that $U = \frac{ds}{dt}$. Using the chain rule $\frac{dU}{dt} = \frac{dU}{ds} \frac{ds}{dt} = U \frac{dU}{ds}$, the equation becomes:

$$mU \frac{dU}{ds} = -\frac{1}{2} C_x \pi \rho R^2 U^2 \implies \frac{dU}{ds} = -\left(\frac{\pi \rho R^2 C_x}{2m}\right) U \quad (5)$$

Defining a characteristic length $\delta = \frac{2m}{\pi \rho R^2 C_x}$, we obtain a first-order differential equation:

$$\frac{dU}{ds} = -\frac{1}{\delta} U \quad (6)$$

The solution is an exponential decay of velocity with distance traveled:

$$U(s) = U_0 e^{-\frac{s}{\delta}}$$

(7)

This theoretical prediction will be tested experimentally to find δ and thus C_x .

3 Experimental Methodology

3.1 Setup and Materials

The experiment involves launching a homogeneous rubber marble ($m = 8.82 \pm 0.01$ g, $R = 10.82 \pm 0.03$ mm) into an aquarium filled with fluid. A custom-built slingshot imparts both translational velocity and backspin to the marble to generate the Magnus effect (Fig. 5).



Figure 5: Slingshot mechanism and marble used for the experiments.

We used two fluids to vary the Reynolds number: tap water and sunflower oil. Their viscosities were measured using a Couette viscometer (Fig. 6).



Figure 6: Experimental measurement of fluid viscosity.

3.2 Trajectory Reconstruction: The Discrete Assumption

The trajectories were recorded using a high-speed camera. To analyze the data using Eq. (7), we need the instantaneous velocity $U(t)$ and the curvilinear abscissa $s(t)$.

The time step between frames is very small ($\tau \approx 4$ ms). This high temporal resolution allows us to make a critical assumption: between two consecutive frames i and $i + 1$, the trajectory segment is approximately straight. Therefore, we do not need to perform a complex continuous integration of the path curve. Instead, we calculate the curvilinear abscissa s via **discrete summation** of Euclidean distances between points.

Let (x_i, y_i) be the coordinates of the marble at frame i . The elementary displacements are:

$$dx_i \approx x_{i+1} - x_i \quad \text{and} \quad dy_i \approx y_{i+1} - y_i \quad (8)$$

The elementary path length is $ds_i = \sqrt{dx_i^2 + dy_i^2}$. The total distance traveled s at frame n is:

$$s_n = \sum_{i=0}^{n-1} ds_i \quad (9)$$

The instantaneous velocity is approximated as $U_i \approx ds_i/\tau$. This discrete approach allows us to linearize the theoretical model for experimental validation:

$$\ln(U(s)) = \ln(U_0) - \frac{1}{\delta} s \quad (10)$$

By plotting $\ln(U)$ against s , we expect a straight line with slope $-1/\delta$.

4 Experimental Results and Analysis

4.1 Experiment 1: Water (High Reynolds Number)

In water ($Re \approx 10^5$, fully turbulent regime), we observed highly curved trajectories, characteristic of strong Magnus forces relative to inertia. Depending on the direction of rotation imparted by the slingshot, we could generate ascending or descending spirals (Fig. 7).



Ascending spiral (\circlearrowleft)

Descending spiral (\circlearrowright)

No rotation (straight)

Figure 7: Various trajectories observed in water.

A chronophotography of an impact in water illustrates the backspin (\circlearrowleft) and the resulting upward curvature (Fig. 8).

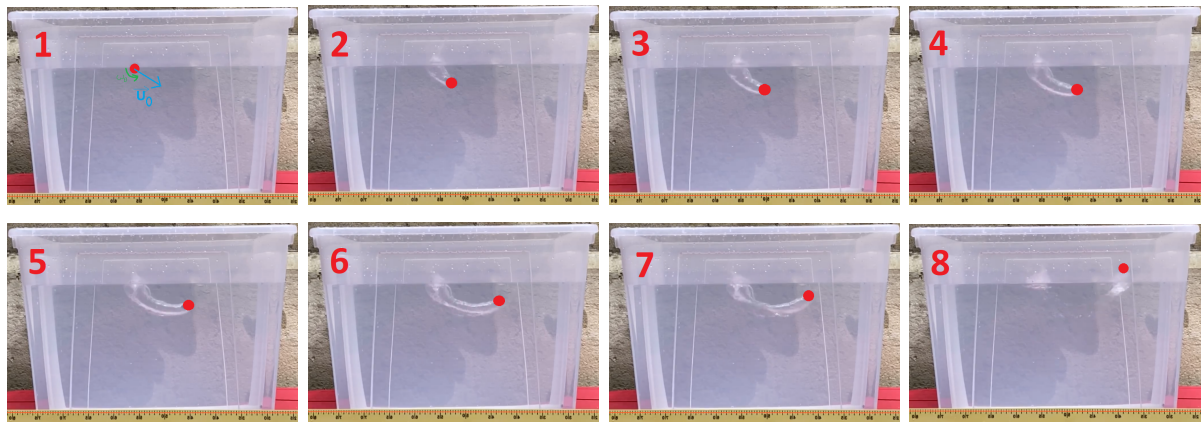


Figure 8: Chronophotography of marble impact in water with counter-clockwise rotation.

Quantitative analysis was performed on a trajectory with initial velocity $U_0 \approx 3.42$ m/s (Fig. 9).

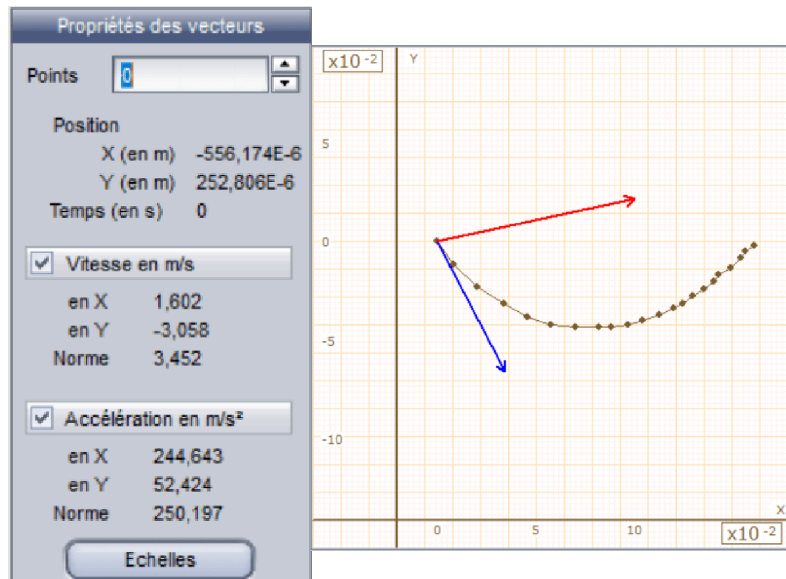


Figure 9: Initial velocity U_0 and acceleration vectors in water (LatisPro).

Using Python to perform linear regression on $\ln(U)$ vs s yields excellent agreement with the theoretical model (Fig. 10).

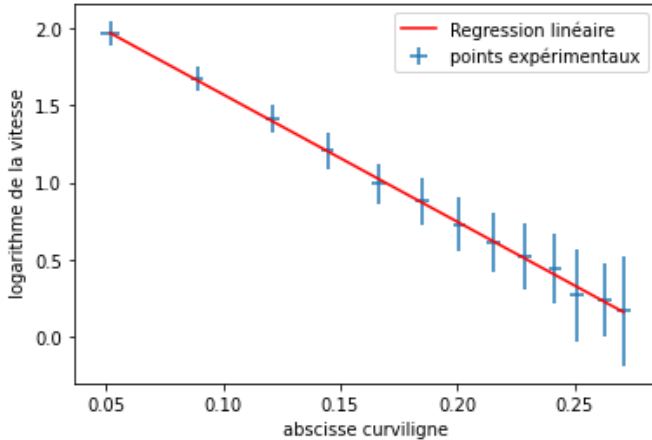


Figure 10: Linear regression $\ln(U)$ vs s for water.

The validity of the fit is confirmed by the Z-score analysis, which remains below 2 for all data points (Fig. 11).

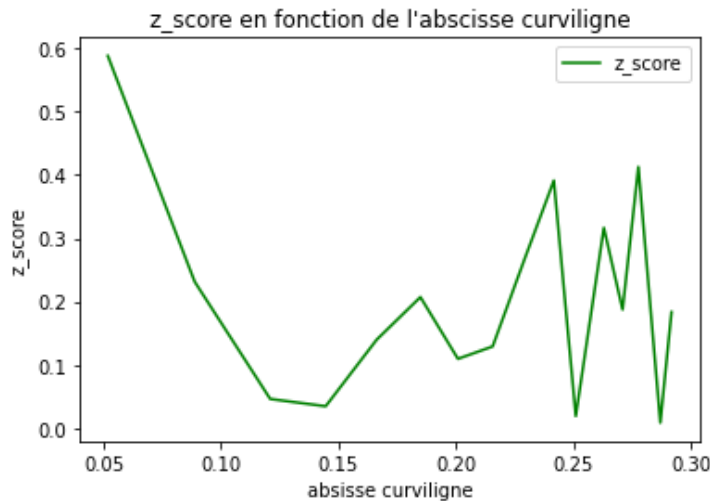


Figure 11: Z_{score} evolution along the trajectory in water.

4.2 Experiment 2: Oil (Moderate Reynolds Number)

We repeated the experiment in oil ($\rho = 900$ g/L, $\eta \approx 81$ mPa.s). The increased viscosity lowers the Reynolds number to $Re \approx 10^3$. The flow remains turbulent, so the quadratic drag model still applies. The chronophotography shows a trajectory that is still curved, but significantly damped compared to water (Fig. 12).

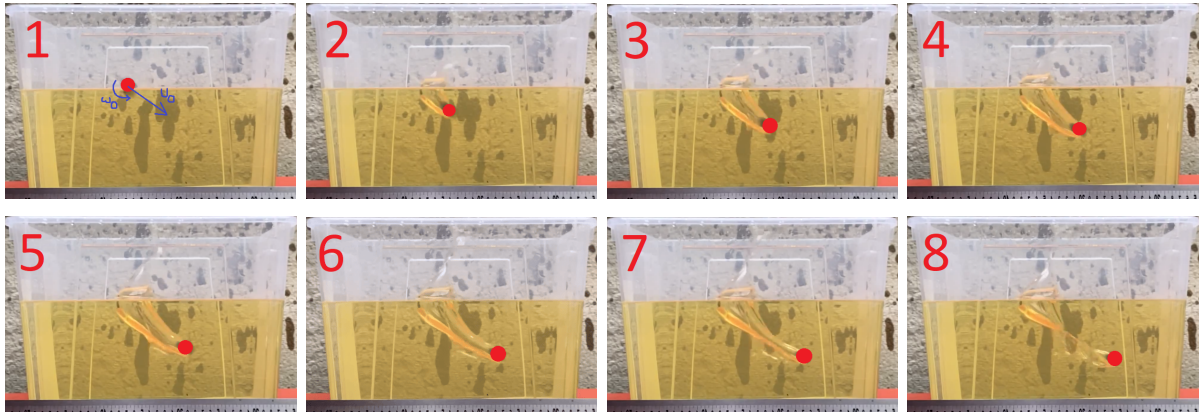


Figure 12: Chronophotography of marble impact in oil with counter-clockwise rotation.

Initial conditions were $U_0 \approx 4.7 \text{ m/s}$ (Fig. 13).

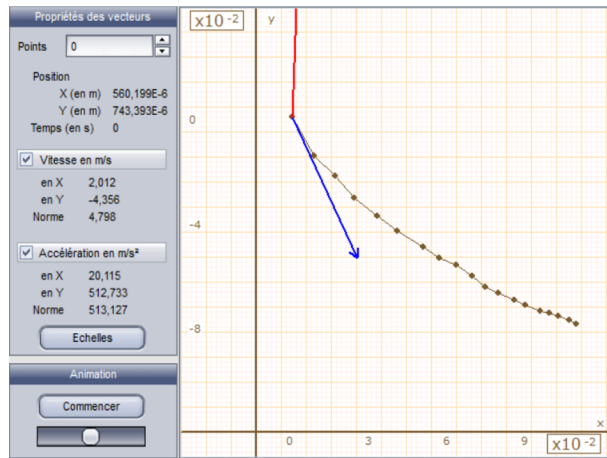
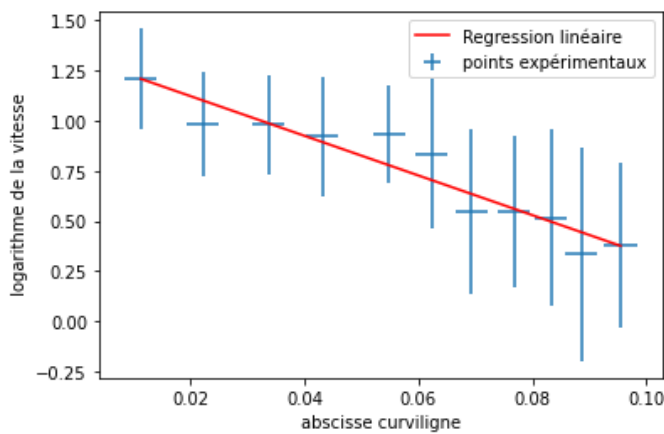


Figure 13: Initial velocity and acceleration vectors in oil.

The linear regression $\ln(U)$ vs s again validates the exponential decay model in this higher viscosity medium (Fig. 14).



Results (Oil):

- Slope $1/\delta \approx (9.24 \pm 0.74) \text{ m}^{-1}$
- Calculated $C_x \approx 0.512 \pm 0.041$
- $z_{score} \approx 1.99$

Figure 14: Linear regression $\ln(U)$ vs s for oil.

The Z-score analysis confirms the model's validity for oil as well (Fig. 15).

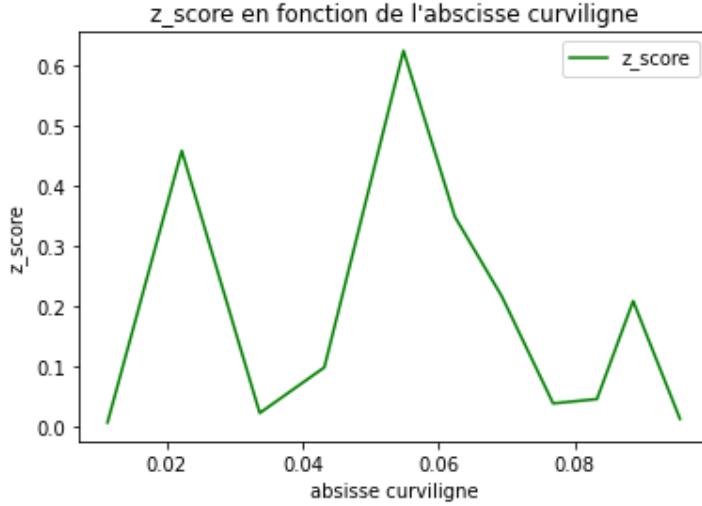


Figure 15: Z_{score} evolution along the trajectory in oil.

4.3 Comparison and Discussion

Comparing the experiments, we find a slightly higher drag coefficient C_x in oil (0.512) than in water (0.426). This is consistent with the standard drag curve for a sphere, where C_x increases as Re decreases from 10^5 towards 10^3 (before the drag crisis region).

Visually, superimposing the trajectories (Fig. 16) shows that while both curve due to Magnus effect, the higher viscosity in oil dampens both translational and rotational velocities more rapidly, leading to a "flatter" trajectory over the same distance.

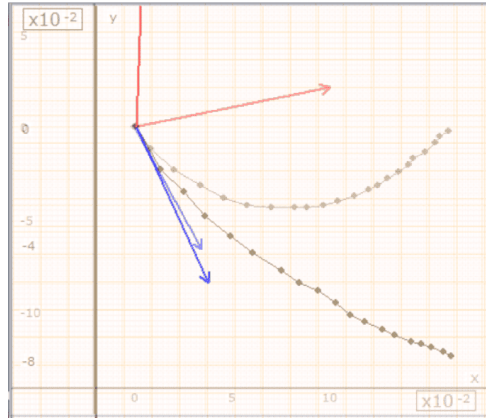


Figure 16: Superposition of tracked trajectories in Water (blue points, sharp curve) and Oil (red points, flatter curve).

5 Conclusion: The Spinning Ball Spiral

Our experiments have successfully demonstrated the physical reality of the Magnus effect and validated the exponential decay of translational velocity caused by fluid drag. By using a discrete summation method for the curvilinear abscissa, enabled by high-speed imaging, we accurately determined drag coefficients in different viscous regimes.

However, answering the initial question—"How to obtain the perfect free-kick"—requires looking beyond simple constant-coefficient models. As highlighted in the extensive work of

Christophe Clanet and colleagues on sports ballistics, the trajectory of a spinning sphere is not a simple circular arc.

Crucially, the translational velocity U and the rotational velocity ω do not decay at the same rate. Drag acts on U , while viscous torque acts on ω . Consequently, the "spin parameter" $S = R\omega/U$, which dictates the magnitude of the lift coefficient, is not constant but evolves along the trajectory.

As the ball slows down translationally (U decreases), the relative importance of rotation often increases initially (increasing S), leading to a tighter curvature. The resulting trajectory is defined by Clanet as a "spinning ball spiral," resembling the shape of a snail shell, which eventually straightens as rotation dies out (Fig. 17).

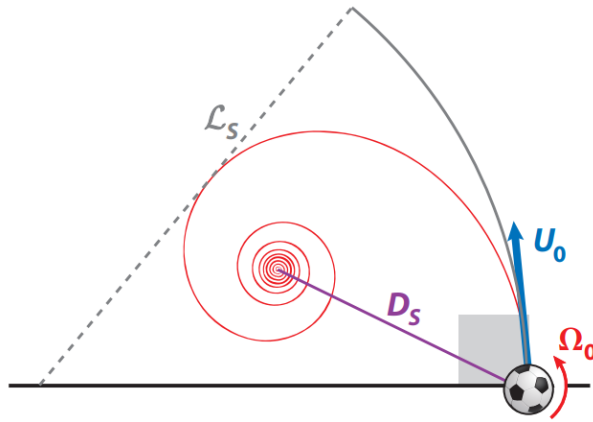


Figure 17: Typical spiral trajectory of a spinning ball resulting from differential decay of U and ω .

Therefore, the "perfect" free-kick is inherently chaotic and difficult to reproduce. It relies on initial conditions (U_0, ω_0 , impact angle) that place the ball on a very specific path within the aerodynamic phase diagram. A minute deviation in the initial kick results in a vastly different spiral trajectory, missing the target. The art of the free-kick lies in the intuitive mastery of these highly sensitive initial conditions to harness the full potential of the Magnus spiral.

Bibliography

1. Christophe Clanet: *Sports Ballistics*, Annual Review of Fluid Mechanics, 2015.
2. Guillaume Dupeux, Caroline Cohen, Anne Le Goff, David Quéré et Christophe Clanet: *Le Football et ses trajectoires*, Reflets de la physique n°28, 2012.
3. Nicolas Plihon, Gauthier Legrand, Francis Pagaud, Arsène Chemin, Jérémie Ferrand, and Nicolas Taberlet: *The physics of Magnus gliders*, 26 August 2021.
4. Ken Bray and David Kerwin: *Modelling the flight of a soccer ball in a direct free kick*, Journal of Sports Sciences, 1 Feb 2003.
5. Christophe Clanet, Guillaume Dupeux et Caroline Cohen: *Football curves*, 2011. Available at researchgate.net.
6. Guillaume Dupeux, Anne Le Goff, David Quéré et Christophe Clanet: *The spinning ball spiral*, New Journal of Physics, 2 September 2010.

A Appendices: Experimental Details and Demonstrations

A.1 Detailed Uncertainty Calculations

The trajectory analysis relies on the discrete measurement of the marble's position frame by frame. Here, we detail the propagation of uncertainty from the coordinate measurements to the final velocity calculation, as presented in the experimental methodology.

A.1.1 Uncertainty on Displacement Vectors

The position of the marble (x_i, y_i) is determined manually on each frame. The estimated uncertainty on the pixel coordinates is:

$$u(x_i) = u(y_i) = 5 \text{ mm} \quad (11)$$

The elementary displacement components are defined as $dx_i = x_{i+1} - x_i$ and $dy_i = y_{i+1} - y_i$. Since the position measurements at steps i and $i + 1$ are independent, the uncertainty on the difference follows the quadratic sum rule:

$$u(dx_i) = \sqrt{u(x_{i+1})^2 + u(x_i)^2} = \sqrt{2}u(x_i) \quad (12)$$

Similarly, $u(dy_i) = \sqrt{2}u(y_i)$.

A.1.2 Uncertainty on the Curvilinear Abscissa (ds_i)

The elementary arc length is given by the Euclidean distance:

$$ds_i = \sqrt{dx_i^2 + dy_i^2} \quad (13)$$

To find the propagation formula, we use the logarithmic differentiation method. Taking the natural logarithm of the equation:

$$\ln(ds_i) = \frac{1}{2} \ln(dx_i^2 + dy_i^2) \quad (14)$$

according to the expression of the differential :

$$df(x, y) = \frac{\partial f}{\partial x}(x, y)dx + \frac{\partial f}{\partial y}(x, y)dy \quad (15)$$

Differentiating both sides yields:

$$\frac{d(ds_i)}{ds_i} = \frac{1}{2} \frac{d(dx_i^2 + dy_i^2)}{dx_i^2 + dy_i^2} = \frac{1}{2} \frac{2dx_i d(dx_i) + 2dy_i d(dy_i)}{dx_i^2 + dy_i^2} \quad (16)$$

Simplifying the expression:

$$\frac{d(ds_i)}{ds_i} = \frac{dx_i}{dx_i^2 + dy_i^2} d(dx_i) + \frac{dy_i}{dx_i^2 + dy_i^2} d(dy_i) \quad (17)$$

To switch from differentials to uncertainties (standard deviations), we apply the Gaussian error propagation law (sum of squares), assuming the errors on dx and dy are uncorrelated:

$$\left(\frac{u(ds_i)}{ds_i} \right)^2 = \left(\frac{dx_i}{dx_i^2 + dy_i^2} u(dx_i) \right)^2 + \left(\frac{dy_i}{dx_i^2 + dy_i^2} u(dy_i) \right)^2 \quad (18)$$

Finally, the absolute uncertainty on the step length is:

$$u(ds_i) = ds_i \sqrt{\left(\frac{dx_i}{dx_i^2 + dy_i^2} u(dx_i) \right)^2 + \left(\frac{dy_i}{dx_i^2 + dy_i^2} u(dy_i) \right)^2} \quad (19)$$

A.3. Uncertainty on Velocity and Logarithmic Velocity

The instantaneous velocity is approximated by $v_i \approx \frac{ds_i}{\tau}$, where τ is the time step between frames. Assuming the uncertainty on the camera timing τ is negligible compared to the spatial measurement error, the relative uncertainty on velocity is equal to the relative uncertainty on distance:

$$\frac{u(v_i)}{v_i} = \frac{u(ds_i)}{ds_i} \quad (20)$$

For the linear regression analysis, we used the natural logarithm of the velocity. The uncertainty on $\ln(v_i)$ is simply the relative uncertainty of v_i :

$$u(\ln(v_i)) = \frac{u(v_i)}{v_i} = \frac{u(ds_i)}{ds_i} \quad (21)$$

This value allows us to calculate the Z-scores to validate the exponential decay model.

A.2 Viscosity Measurement Principle

Viscosity was measured using a Couette viscometer. By measuring the resistive torque Γ on an inner cylinder rotating at ω inside an outer cylinder containing the fluid, viscosity η is derived from the Navier-Stokes equations in cylindrical coordinates (ignoring end effects):

$$\eta = \frac{\Gamma_{motor}a}{R^3 2\pi H \omega} \quad (22)$$

Where a is the gap width, R the radius, and H the height of the immersed cylinder.

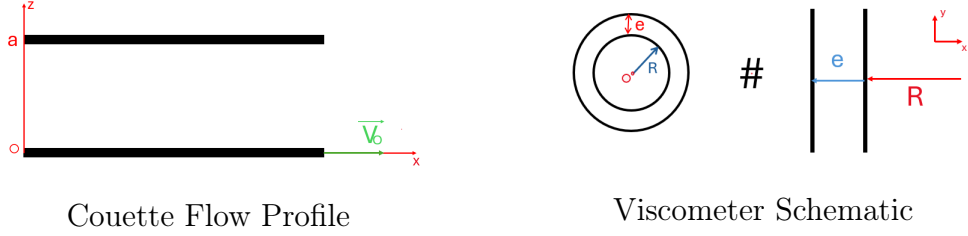


Figure 18: Principle of Couette viscometry.